Supporting information

# Enhanced Visible-NIR Absorption and Oxygen Vacancy Generation of Pt/$H_xMoWO_y$ by H-spillover to Facilitate Photothermal Catalytic $CO_2$ Hydrogenation

*Hao Ge,[a] Yasutaka Kuwahara,*[a,b,c,d] Kazuki Kusu,[a] Hisayoshi Kobayashi,[a,e] Hiromi Yamashita*[a,b,c]*

[a] Division of Materials and Manufacturing Science, Graduate School of Engineering, Osaka University, 2-1 Yamada-oka, Osaka 565-0871, Japan

[b] Institute for Open and Transdisciplinary Research Initiatives (OTRI), Osaka University, 2-1 Yamada-oka, Suita, Osaka 565-0871, Japan

[c] Unit of Elements Strategy Initiative for Catalysts & Batteries (ESICB), Kyoto University, Katsura, Kyoto 615-8520, Japan

[d] JST, PRESTO, 4-1-8 Hon-Cho, Kawaguchi, Saitama 332-0012, Japan

[e] Kyoto Institute of Technology, Matsugasaki, Sakyo-ku, Kyoto 606-8585, Japan

*E-mail: kuwahara@mat.eng.osaka-u.ac.jp (Y. Kuwahara);

yamashita@mat.eng.osaka-u.ac.jp (H. Yamashita)

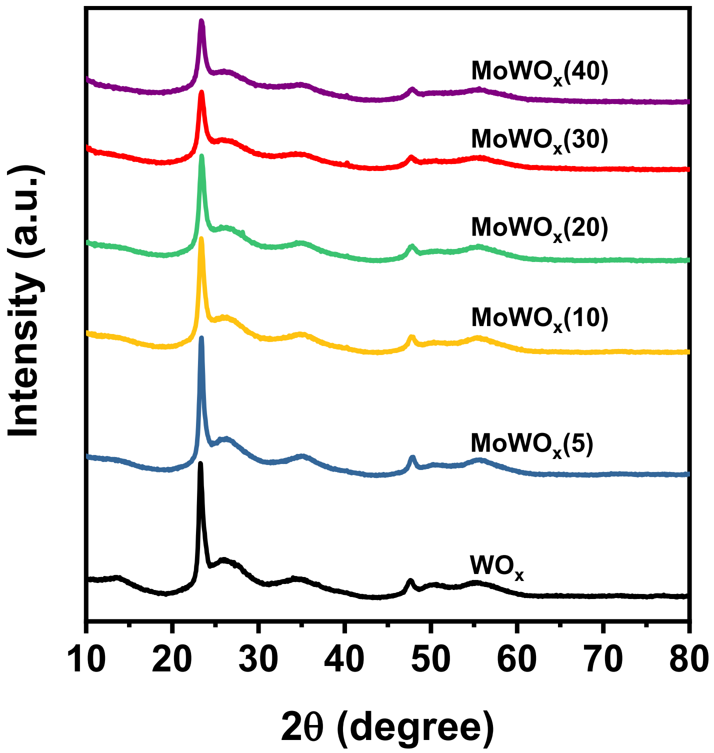


**Fig. S1** XRD patterns of $WO_y$ and $MoWO_y$ with different ratios of Mo-doping (z = 5~40).

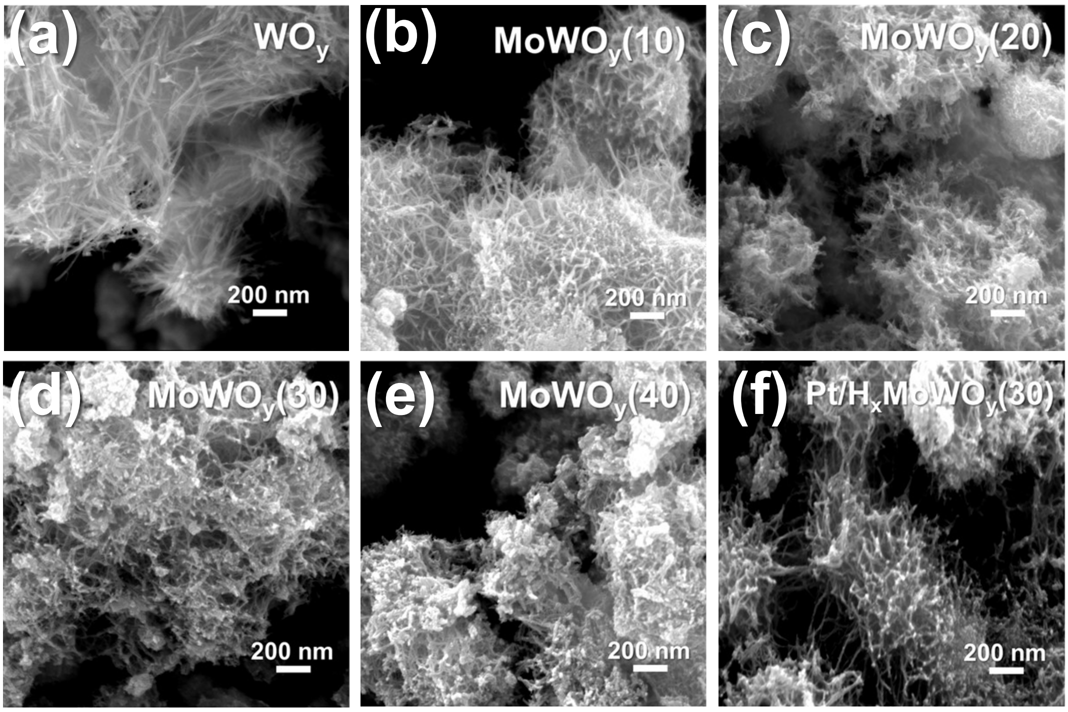


**Fig. S2** FE-SEM images of WO$_y$, MoWO$_y$(5), MoWO$_y$(10), MoWO$_y$(20), MoWO$_y$(30), MoWO$_y$(40) and Pt/H$_x$MoWO$_y$(30).

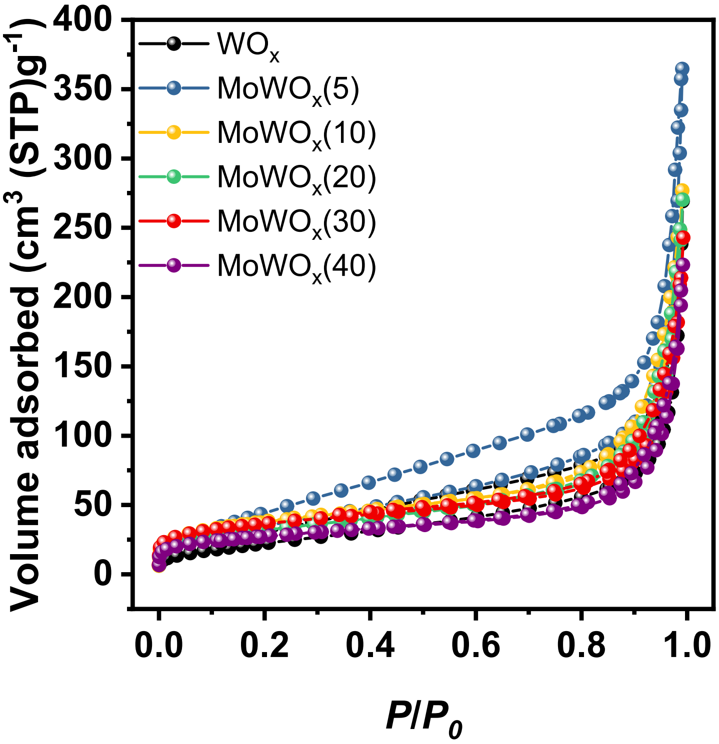


**Fig. S3** Nitrogen adsorption-desorption isotherms for $WO_y$, $MoWO_y$(5), $MoWO_y$(10), $MoWO_y$(20), $MoWO_y$(30) and $MoWO_y$(40), respectively.

**Table S1.** The specific BET surface area of pure $WO_y$ and $MoWO_y$(z) with different ratios of Mo-doping (z = 5~40).

| Catalyst | BET surface area ($m^2/g$) |
|---|---|
| $WO_y$ | 87.8 |
| $MoWO_y$(5) | 135 |
| $MoWO_y$(10) | 127 |
| $MoWO_y$(20) | 118 |
| $MoWO_y$(30) | 111 |
| $MoWO_y$(40) | 89.5 |

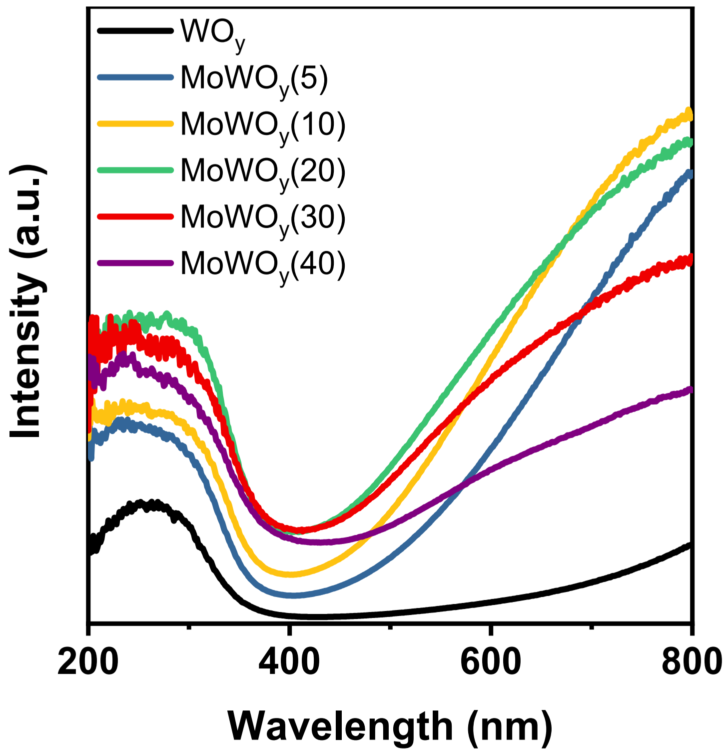


**Fig. S4** UV-vis-NIR diffuse reflectance spectra of $MoWO_y$(z) with different amounts of Mo-doping (z = 5~40) and pure $WO_y$.

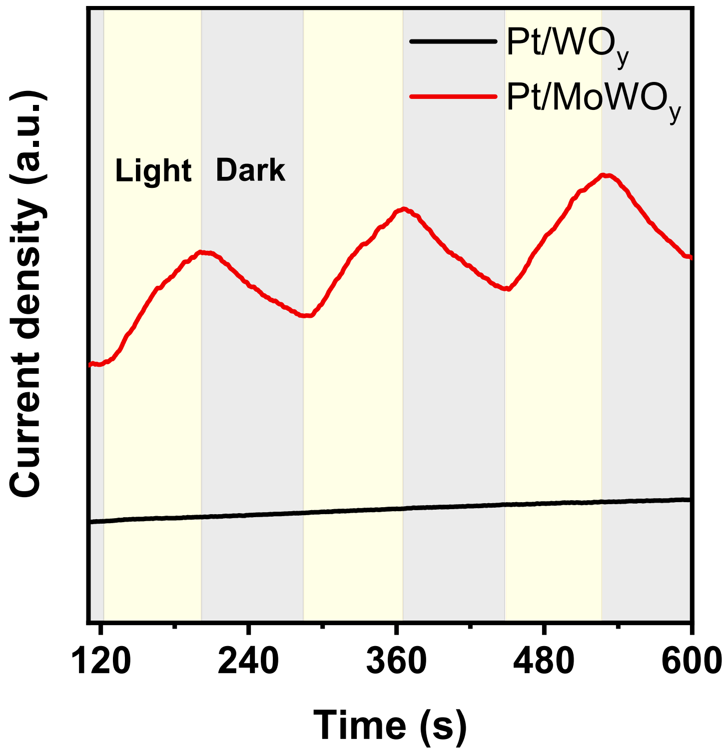


**Fig. S5** Photoelectrochemical measurement of Pt/$WO_y$ and Pt/$MoWO_y$. (Light source : Xe lamp, Intensity = 0.88 W $cm^{-2}$, $\lambda$ > 450 nm)

**Table S2.** ICP analysis results for the weight percentage of doped Mo element and deposited Pt in Pt/MoWO$_y$(z) (z = 0~40) samples.

| Sample | Mo | | Pt | |
|---|---|---|---|---|
| | Expected (wt%) | Exp. (wt%) | Expected (wt%) | Exp. (wt%) |
| Pt/WO$_y$ | - | - | 2.9 | 1.5 |
| Pt/MoWO$_y$(5) | 2.0 | 1.7 | 2.9 | 1.4 |
| Pt/MoWO$_y$(10) | 4.0 | 3.3 | 2.9 | 1.5 |
| Pt/MoWO$_y$(20) | 7.7 | 5.1 | 2.9 | 1.8 |
| Pt/MoWO$_y$(30) | 11 | 7.2 | 2.9 | 1.9 |
| Pt/MoWO$_y$(40) | 14 | 9.7 | 2.9 | 2.2 |

**Table S3.** Summary of the results of CO pulse measurement for a series of Pt/$H_x$MoW$O_y$(z) (z = 0~40) catalysts synthesized with the same Pt loading.

| Sample | Volume of CO adsorbed [$cm^3$/g-sample] | Metal dispersion [%] | Surface area of metal [$m^2$/g-sample] | Average diameter of metal particle [nm] |
|---|---|---|---|---|
| Pt/W$O_y$ | 0.21 | 12.5 | 30.5 | 9.2 |
| Pt/$H_x$MoW$O_y$(5) | 0.21 | 11.9 | 29.6 | 9.4 |
| Pt/$H_x$MoW$O_y$(10) | 0.23 | 11.7 | 29.1 | 9.6 |
| Pt/$H_x$MoW$O_y$(20) | 0.24 | 12.8 | 31.7 | 8.9 |
| Pt/$H_x$MoW$O_y$(30) | 0.27 | 12 | 29.7 | 9.4 |
| Pt/$H_x$MoW$O_y$(40) | 0.24 | 11 | 26.9 | 10.7 |

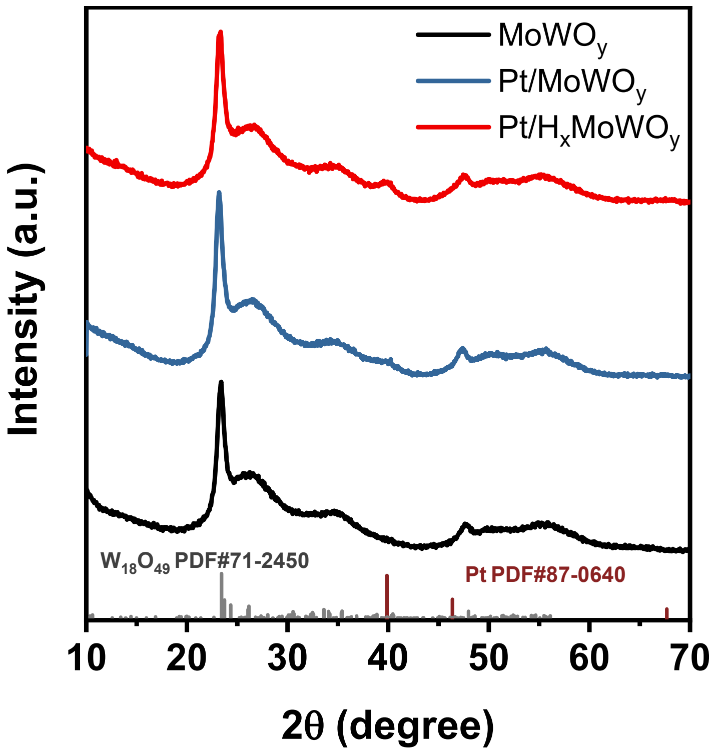


**Fig. S6** XRD patterns of $MoWO_y$, $Pt/MoWO_y$, and $Pt/H_xMoWO_y$.

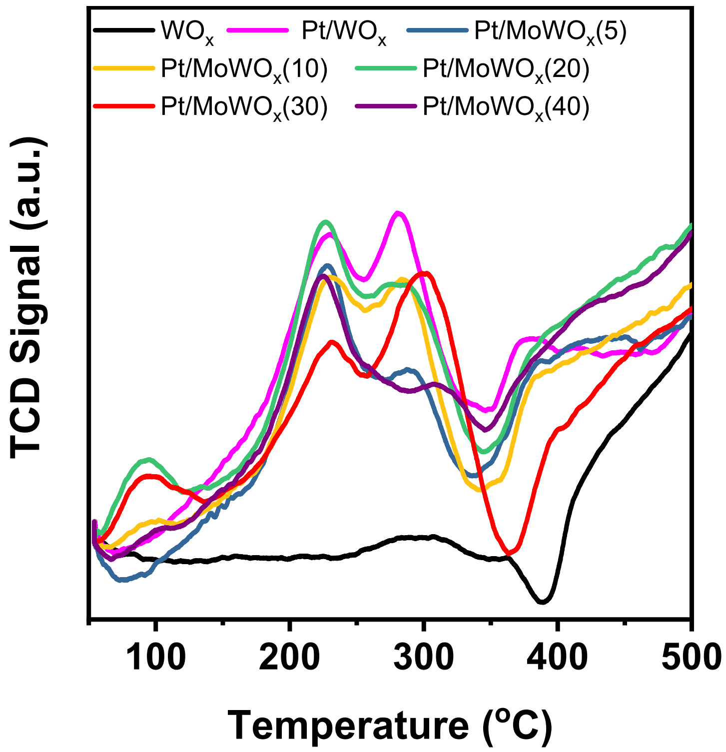


**Fig. S7** $H_2$ temperature-programmed reduction ($H_2$-TPR) profiles of Pt/Mo$WO_y$(z) (z = 0~40) and pure $WO_y$.

**Table S4.** Summary of XPS measurement results of W 4*f* for the Pt/$WO_y$, Pt/$MoWO_y$, Pt/$H_xWO_y$ and Pt/$H_xMoWO_y$.

| Sample | W 4*f* XPS | | | |
|---|---|---|---|---|
| | $W^{4+}$ (at%) | $W^{5+}$ (at%) | $W^{6+}$ (at%) | $W^{4+}/W_{total}$ (at%) |
| Pt/$WO_y$ | 17 | 25 | 57 | 17 |
| Pt/$MoWO_y$ | 18 | 35 | 58 | 18 |
| Pt/$H_xWO_y$ | 18 | 31 | 51 | 18 |
| Pt/$H_xMoWO_y$ | 22 | 35 | 43 | 22 |

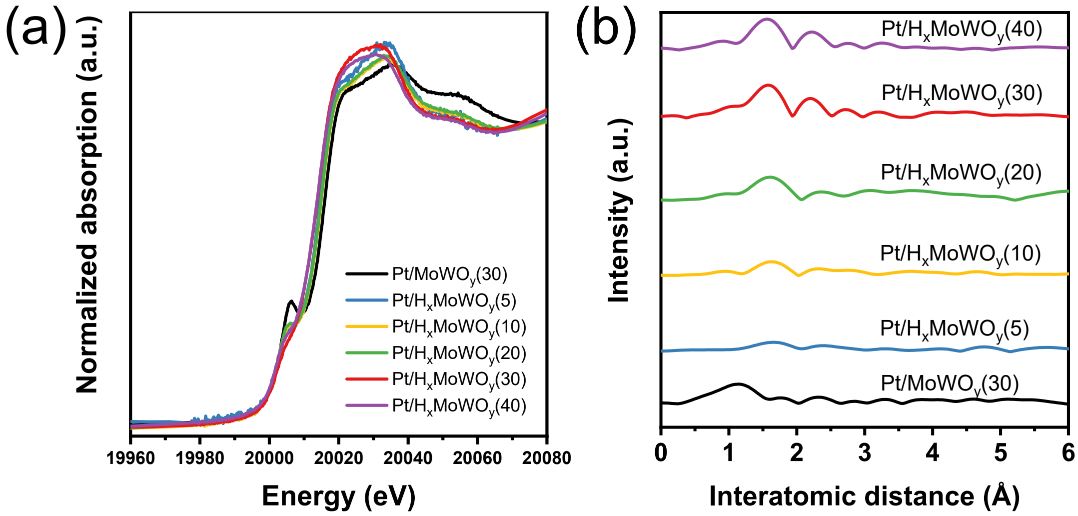


**Fig. S8** (a) XANES spectra and (b) FT-EXAFS spectra at the Mo K-edge of unreduced Pt/MoWO$_y$ and Pt/H$_x$MoWO$_y$(z) with different amounts of Mo-doping (z = 5~40).

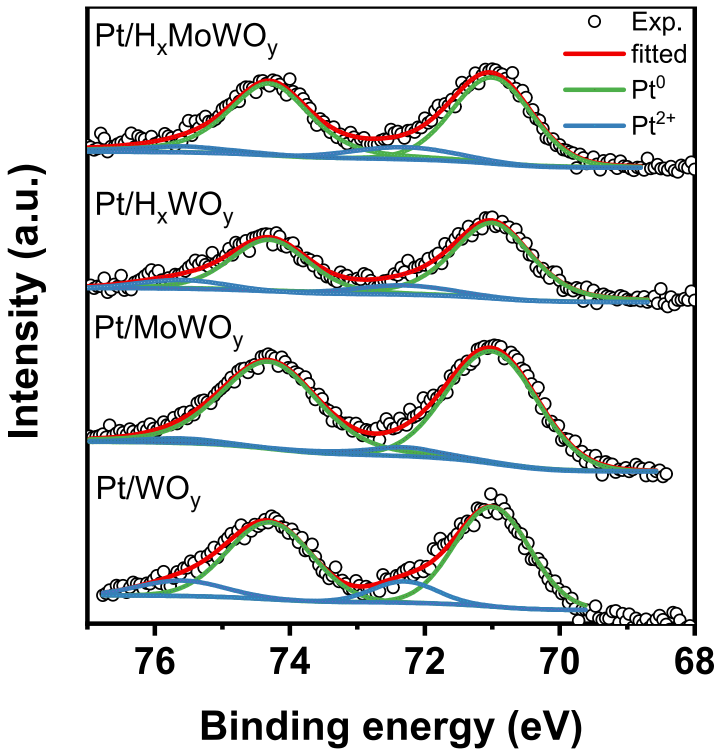


**Fig. S9** Pt 4*f* XPS spectra of Pt/WO$_y$, Pt/MoWO$_y$, Pt/H$_x$WO$_y$ and Pt/H$_x$MoWO$_y$.

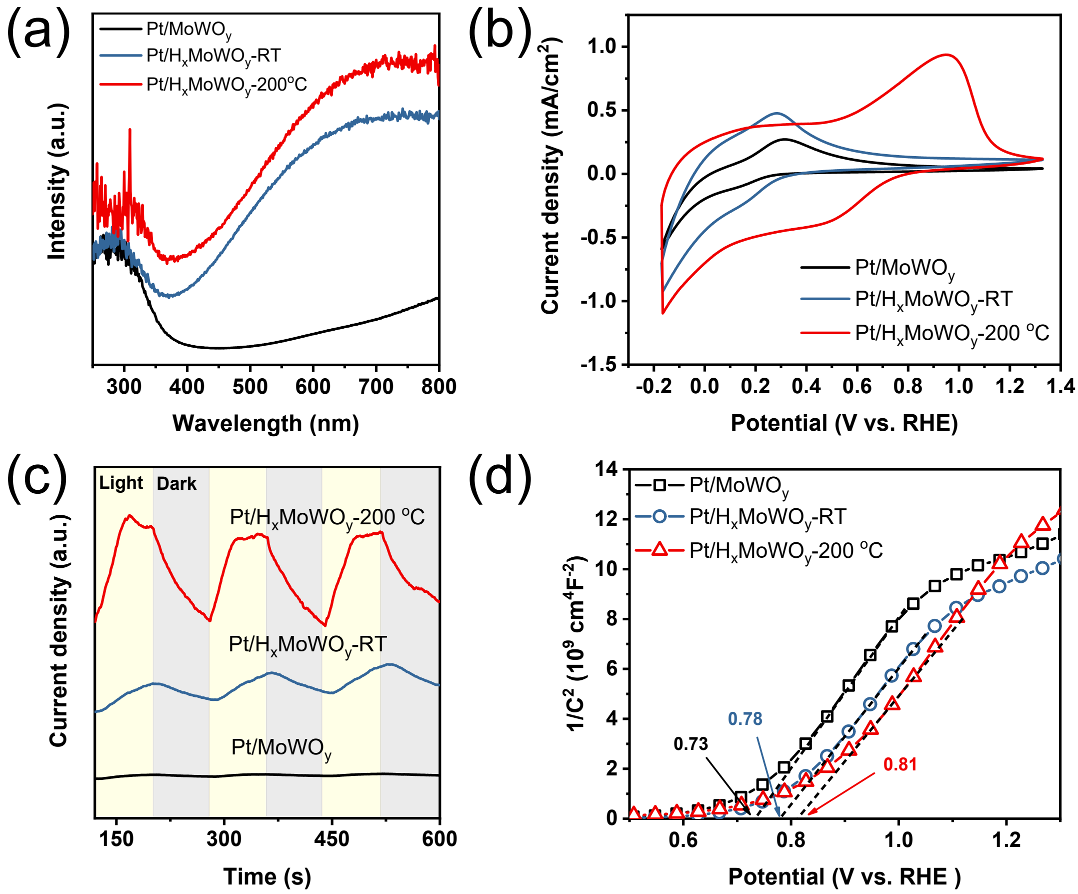


**Fig. S10** (a) UV-vis-NIR diffuse reflectance spectra, (b) CV profiles, (c) photocurrent measurement and (d) Mott-Schottky plots of Pt/$H_xMoWO_y$ with different $H_2$ reduction temperature (Light source: Xe lamp, Intensity = 0.88 W cm$^{-2}$, $\lambda > 450$ nm).

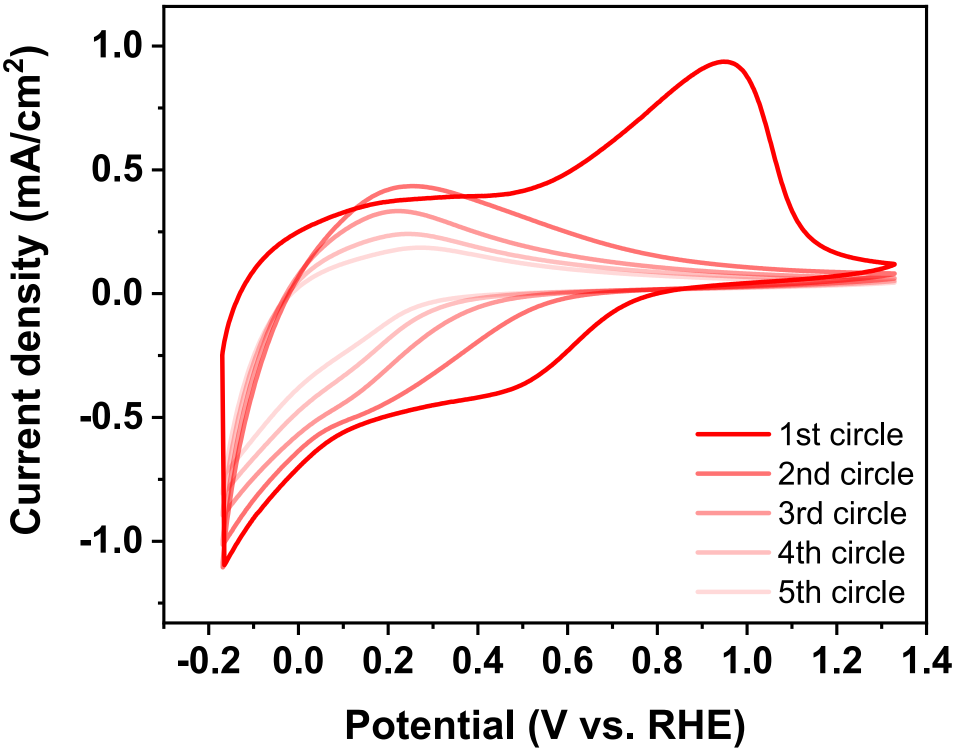


**Fig. S11** CV profiles of Pt/$H_x$Mo$WO_y$ with repeated five cycles.

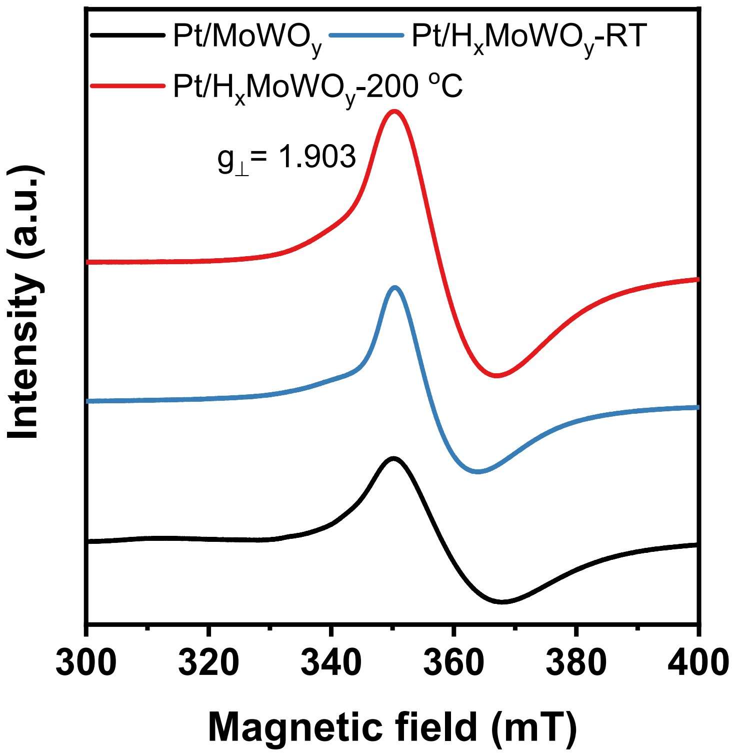


**Fig. S12** ESR spectrum of of Pt/$H_xMoWO_y$ with different $H_2$ reduction temperature.

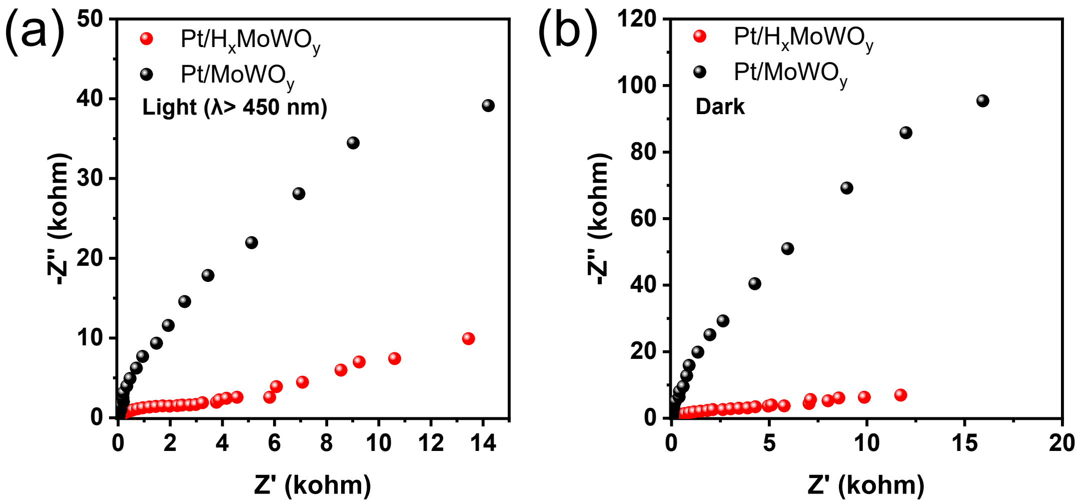


**Fig. S13** Impedance curves of Pt/$H_xMoWO_y$ and Pt/$MoWO_y$ under (a) light and (b) dark conditions.

**Table S5.** Performance comparison of different photocatalysts for RWGS reaction.

| Catalyst | Gas ($CO_2$ : $H_2$) | Light Source | Temp. (°C) | CO production rate | Ref. |
|---|---|---|---|---|---|
| Pd@$WO_3$ | 1:1 | 300W Xe lamp | 250 | 3 mmol $g^{-1}$ $h^{-1}$ | 1 |
| Rh/$Al_2O_3$ | 1:1 | 300W Xe lamp | 360 | 96.5% | 2 |
| $In_2O_{3-x}(OH)_y$ | 1:1 | 1000W metal halide bulb | 150 | 1.2 μmol $g^{-1}h^{-1}$ | 3 |
| Pt/$NaTaO_3$ | 1:1 | 300W UV-enhanced Xe lamp | - | 139.1 μmol $g^{-1}h^{-1}$ | 4 |
| Pd@$Nb_2O_5$ | 1:1 | 300W Xe lamp | - | 1.8 mmol $g^{-1}$ $h^{-1}$ | 5 |
| $In_2O_{3-x}$ nanosheet | 1:1 | 300W Xe lamp | 340 | 103.21 mmol $g^{-1}$ $h^{-1}$ | 6 |
| C-$In_2O_3$ | 1:1 | 300W Xe lamp | 340 | 123.41 mmol $g^{-1}$ $h^{-1}$ | 7 |
| ncSi:H | 1:1 | 300W Xe lamp | 150 | 250 μmol $g^{-1}h^{-1}$ | 8 |
| $Bi_2O_{3-x}$ | 1:1 | LED lamp | - | 16.1 μmol $g^{-1}$ $h^{-1}$ | 9 |
| Pt/$H_xMoO_{3-y}$(Sheet) | 1:1 | 500W Hg-Xe short arc lamp | 140 | 1.2 mmol $g^{-1}$ $h^{-1}$ | 10 |
| Pt/$H_xMoWO_y$ | 1:1 | 500W Hg-Xe short arc lamp | 140 | 3.1 mmol $g^{-1}$ $h^{-1}$ | This work |

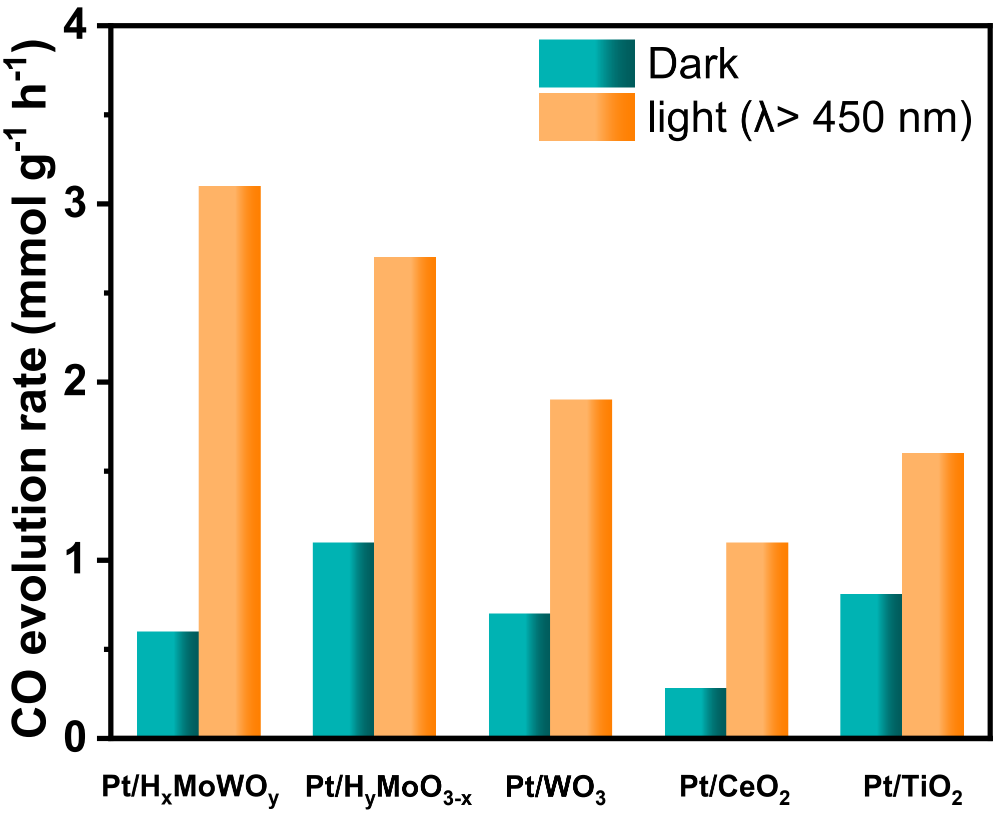


**Fig. S14** Comparison of catalytic performance of various oxide-supported Pt catalysts in photothermal catalytic RWGS reaction. (Reaction conditions: catalyst (0.1 g), $H_2/CO_2$ (1 : 1, total 20 mL min$^{-1}$), Xe lamp (λ > 450 nm), Reaction Temp. = 140 $^{o}$C, Light intensity: 0.88 W cm$^{-2}$)

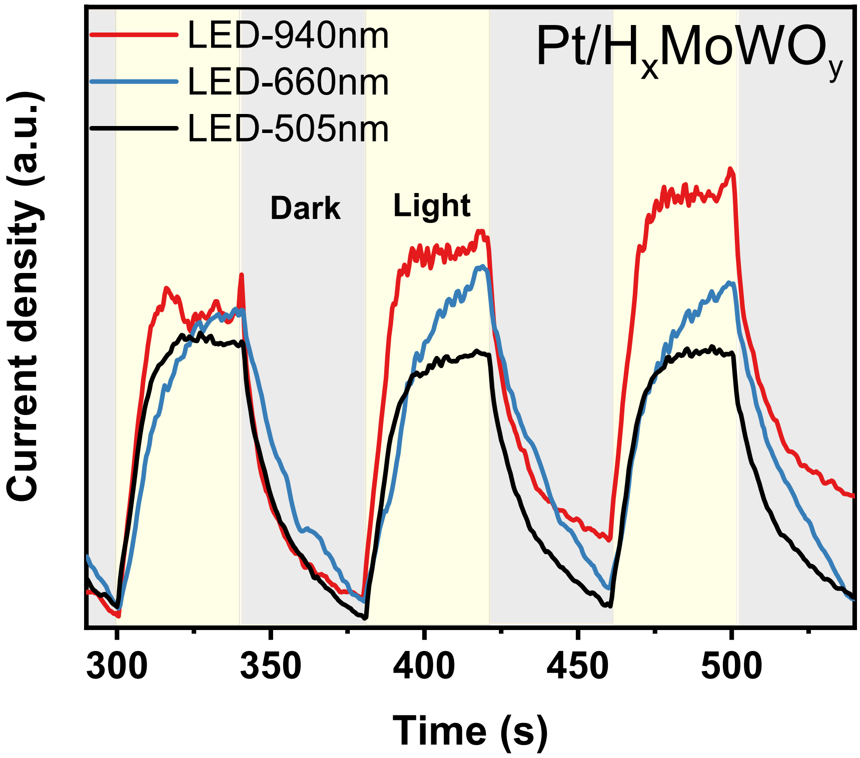


**Fig. S15** Photocurrent measurement of Pt/$H_x$MoWO$_y$ with different LED lamp irradiation.

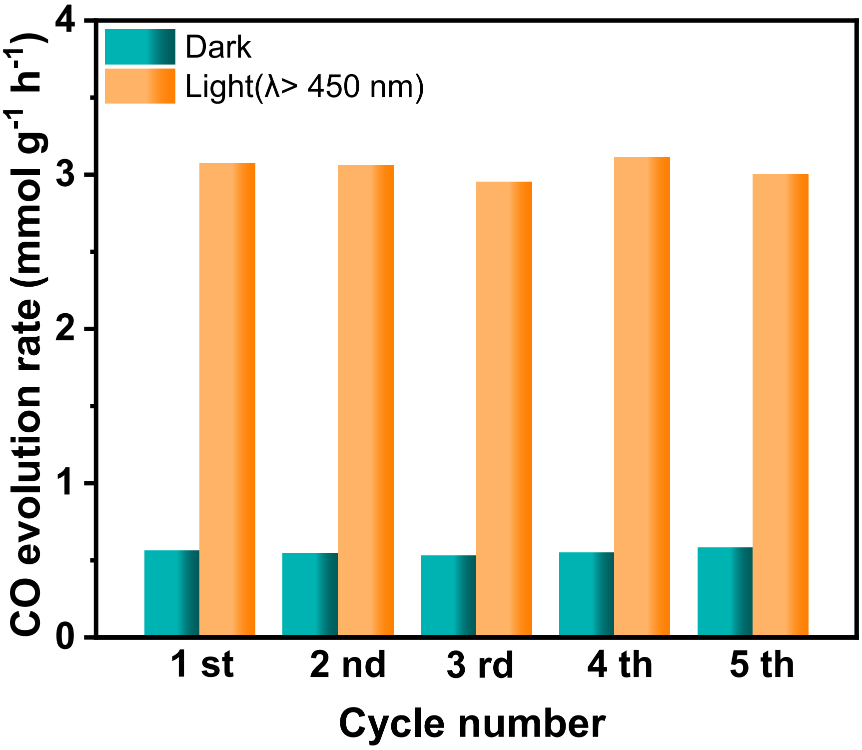


**Fig. S16** The cycle test of Pt/$H_xMoWO_y$ for photothermal catalytic $CO_2$ reduction in a flowing system (reaction conditions: catalyst (0.1 g), $H_2/CO_2$ (10/10 mL/min), light source: λ > 450 nm, reaction temp.: 140 °C)

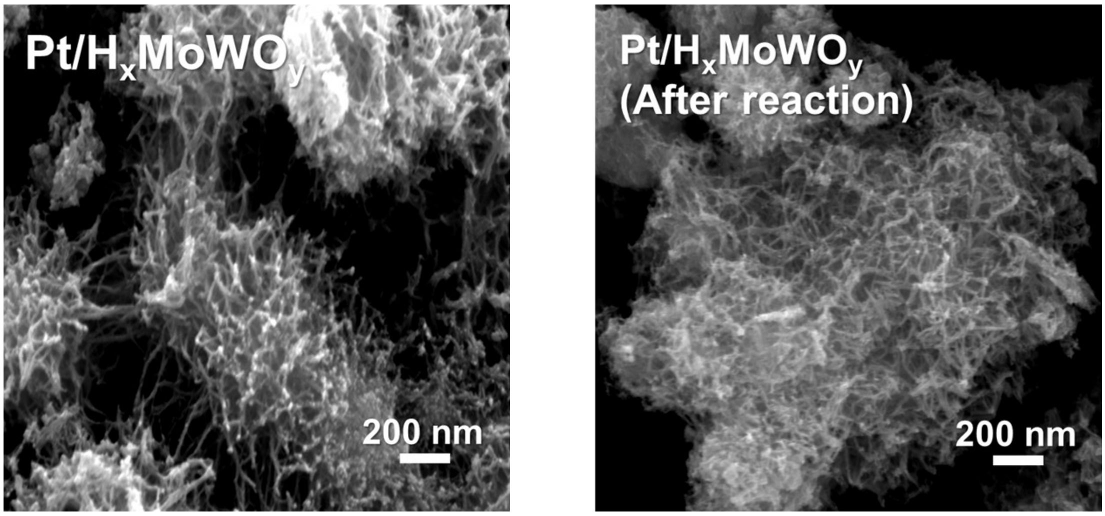


**Fig. S17** FE-SEM images of Pt/$H_x$MoW$O_y$ before and after reaction.

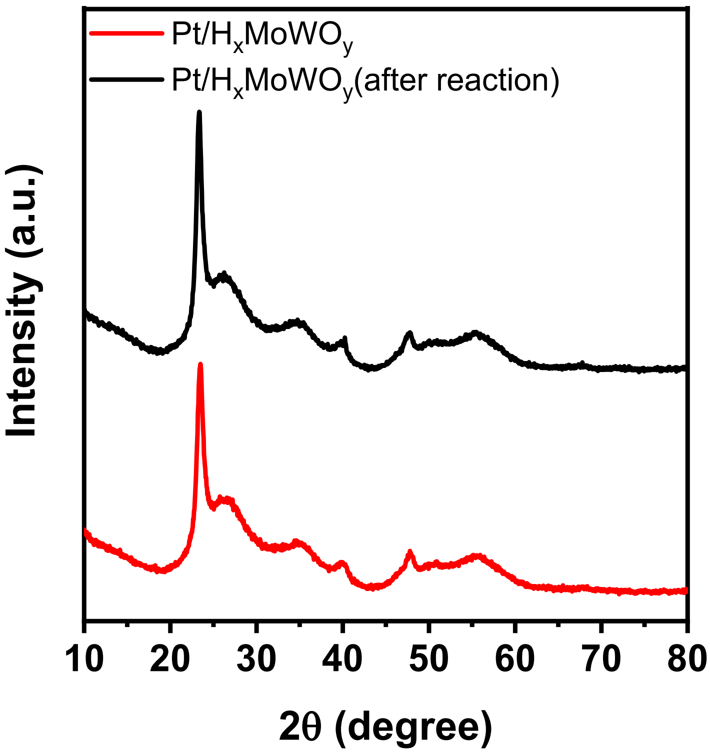


**Fig. S18** XRD patterns of Pt/$H_x$MoW$O_y$ before and after reaction.

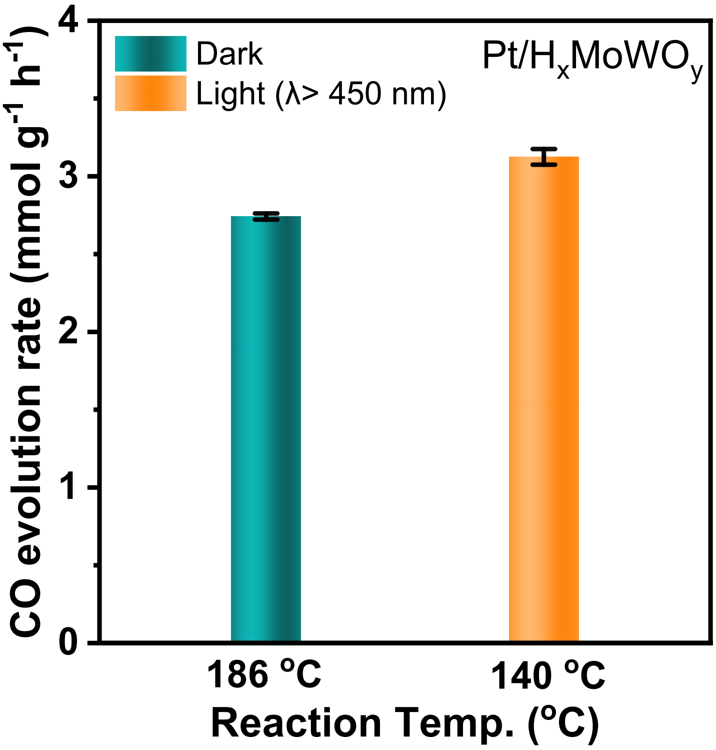


**Fig. S19** Photothermal catalytic performance test in the reverse water-gas shift (RWGS) reaction under the dark condition and Vis-NIR irradiation: CO evolution rate on Pt/$H_xMoWO_y$ with different reaction temperature.

**Table S6.** The amount of oxygen vacancy on the surface in Pt/MoWO$_y$(z) after $H_2$ reduction.

| Sample | The amount of surface oxygen vacancy (μmol/g-cat) |
|---|---|
| Pt/WO$_y$-$H_2$ | 245 |
| Pt/H$_x$MoWO$_y$(5) | 274 |
| Pt/H$_x$MoWO$_y$(10) | 356 |
| Pt/H$_x$MoWO$_y$(20) | 439 |
| Pt/H$_x$MoWO$_y$(30) | 572 |
| Pt/H$_x$MoWO$_y$(40) | 512 |

Determination of surface oxygen vacancy

The oxygen vacancy on the surface of the catalyst can capture the oxygen of the diphenyl sulfoxide to produce diphenyl sulfide. The oxygen vacancy in $MoO_3$ cannot be regenerated in dark without $H_2$ gas. The reaction will stop when the surface oxygen vacancy of $MoO_3$ is exhausted. Therefore, this reaction can be used to calculate the number of surface oxygen vacancies with different morphologies of $MoO_3$ by counting the yield of diphenyl sulfide. The reaction operation as follows: First, add 50 mg catalyst to the quartz tube and seal the nozzle for $H_2$ reduction with the temperature of 200 °C, and the hydrogen reduction process was maintained for 30 minutes. After that, argon gas is introduced into the quartz tube for 20 minutes to expel the hydrogen. And add the reaction solution into the quartz tube (Diphenyl sulfoxide:0.2mmol; Diphenyl: 0.1mmol; Methylbenzene: 10mL). Finally, 0.1mL of the reaction solution is taken out and analyzed by GC.

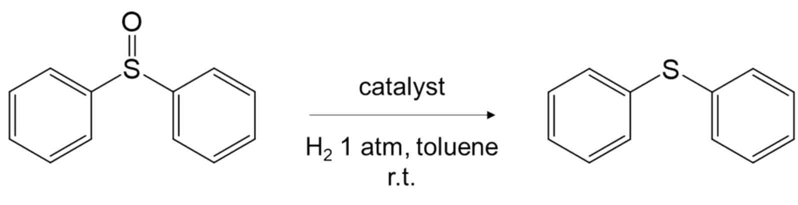


**Scheme S1.** Deoxygenation of diphenyl sulfoxide to phenyl sulfide using molecular $H_2$ as a reductant.

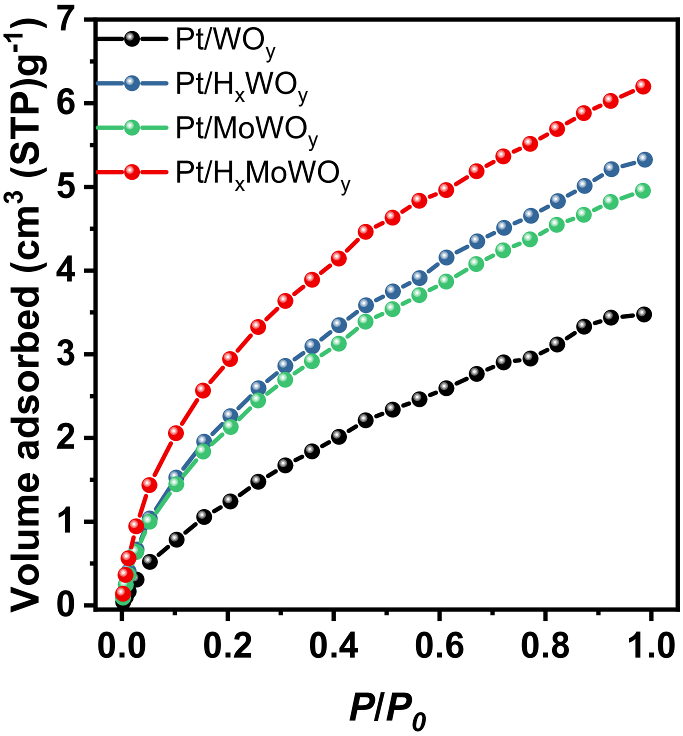


**Fig. S20** $CO_2$ adsorption isotherms measured at 25 °C for Pt/MoWO$_y$ and Pt/WO$_y$ before and after $H_2$ reduction.

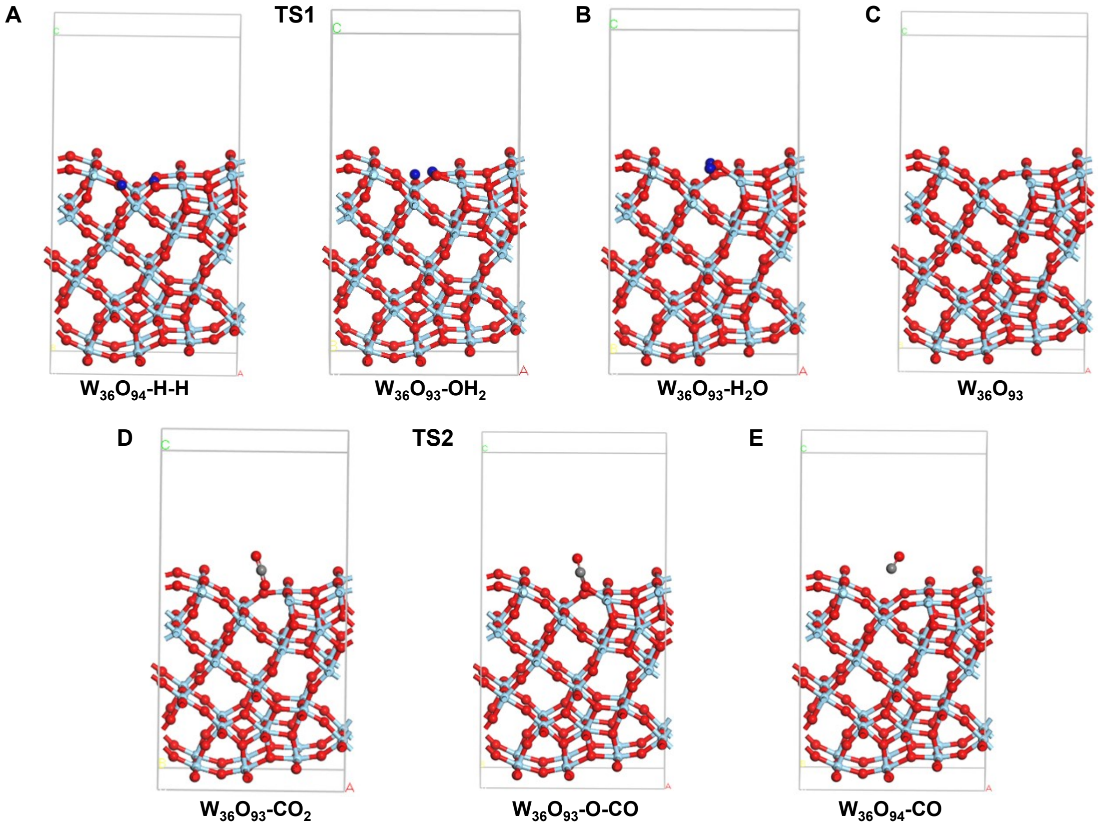


**Fig. S21** The detailed structure models in each reaction step of $CO_2$ hydrogenation to produce CO on $W_{36}O_{94}$ model.

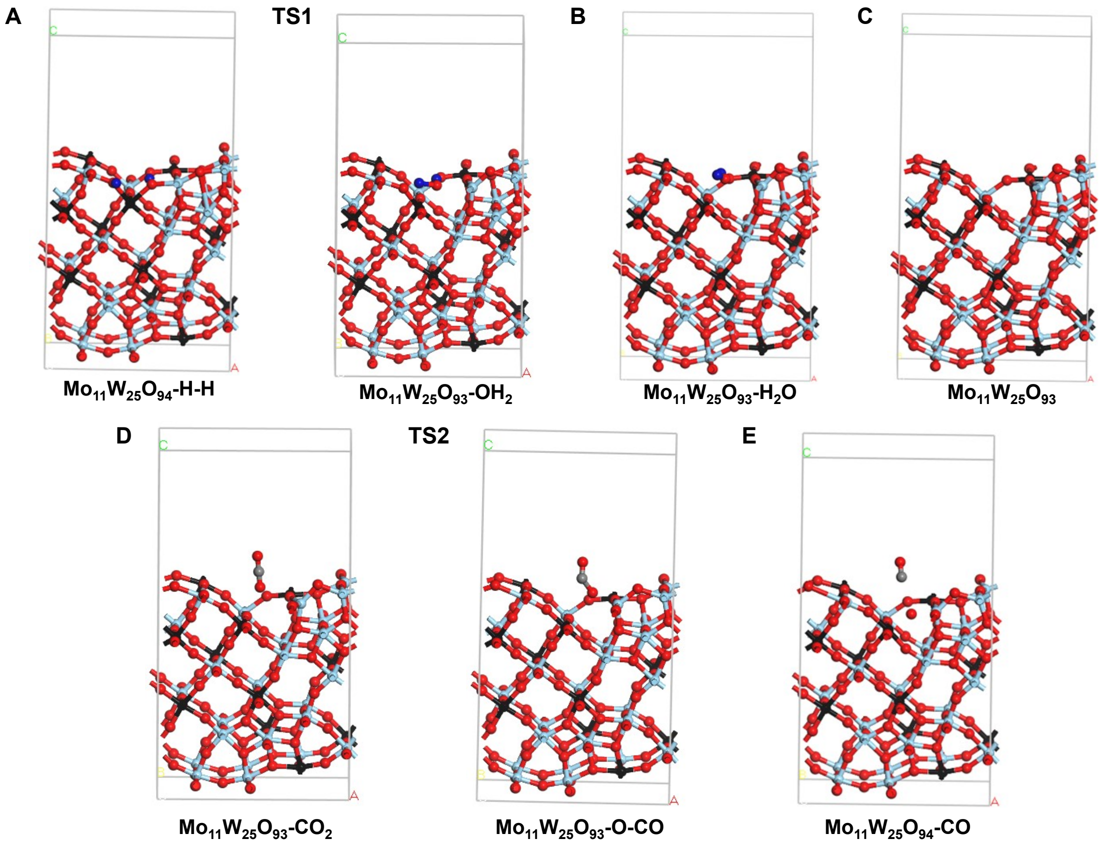


**Fig. S22** The detailed structure models in each reaction step of $CO_2$ hydrogenation to produce CO on $Mo_{11}W_{25}O_{94}$ model.

**Table S7.** Summary of the XPS measurement results of W 4*f* for the Pt/$H_xMoWO_y$, Pt/$H_xMoWO_y$→$CO_2$ and Pt/$H_xMoWO_y$→$CO_2$→$H_2$.

| Sample | W 4*f* XPS | | | |
|---|---|---|---|---|
| | $W^{4+}$ (at%) | $W^{5+}$ (at%) | $W^{6+}$ (at%) | $W^{4+}$ /$W_{total}$ (at%) |
| Pt/$H_xMoWO_y$ | 22 | 35 | 43 | 22 |
| Pt/$H_xMoWO_y$→$CO_2$ | 0 | 24 | 76 | 0 |
| Pt/$H_xMoWO_y$→$CO_2$→$H_2$ | 5 | 36 | 59 | 5 |

**Table S8.** Summary of the XPS measurement results of Mo 3*d* for the Pt/$H_xMoWO_y$, Pt/$H_xMoWO_y$→$CO_2$ and Pt/$H_xMoWO_y$→$CO_2$→$H_2$.

| Sample | Mo 3*d* XPS | | | |
|---|---|---|---|---|
| | $Mo^{4+}$ (at%) | $Mo^{5+}$ (at%) | $Mo^{6+}$ (at%) | ($Mo^{4+}$ + $Mo^{5+}$)/$Mo_{total}$ (at%) |
| Pt/ $H_xMoWO_y$ | 22 | 78 | 0 | 100 |
| Pt/ $H_xMoWO_y$→$CO_2$ | 0 | 48 | 52 | 48 |
| Pt/$H_xMoWO_y$→$CO_2$→$H_2$ | 0 | 70 | 30 | 70 |

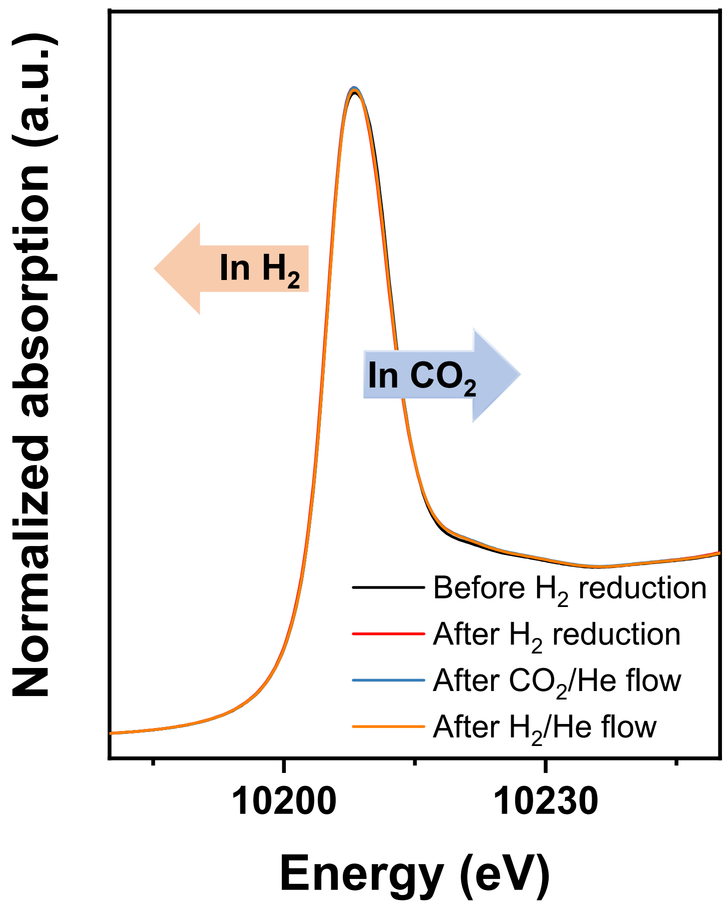


**Fig. S23** *In situ* W L3-edge XANES spectra of Pt/$H_xMoWO_y$; before $H_2$ reduction, after $H_2$ reduction under a flow of 20% $H_2$/He (reduction temp.: 200 °C), after subsequent flow of 20% $CO_2$/He and subsequent flow of 20% $H_2$/He (measured at 140 °C).

## References


1 Y. F. Li, N. Soheilnia, M. Greiner, U. Ulmer, T. Wood, A. A. Jelle, Y. Dong, A. P. Yin Wong, J. Jia and G. A. Ozin. *ACS Appl. Mater. Interfaces,* 2019, **11** (6), 5610–5615.

2 X. G. Meng, T. Wang, L. Q. Liu, S. X. Ouyang, P. Li, H. L. Hu, T. Kako, H. Iwai, A. Tanaka, J. H. Ye. *Angew. Chem. Int. Ed.* 2014, **53** (43), 11478-11482.

3 L. He, T. E. Wood, B. Wu, Y. C. Dong, L. B. Hoch, L. M. Reyes, D. Wang, C. Kubel, C. X. Qian, J. Jia, K. Liao, P. G. O'Brien, A. Sandhel, J. Y. Y. Loh, P. Szymanski, N. P. Kherani, T. C. Sum, C. A. Mims, G. A. Ozin. *ACS Nano.* 2016, **10** (5), 5578-5586.

4 J. Jia, P. G. O'Brien, L. He, Q. Qiao, T. Fei, L. M. Reyes, T. E. Burrow, Y. C. Dong, K. Liao, M. Varela, S. J. Pennycook, M. Hmadeh, A. S. Helmy, N. P. Kherani, D. D. Perovic, G. A. Ozin. *Adv. Sci.* 2016, **3** (10), 1600189 (13 pages).

5 H. B. Zhang, T. Wang, J. J. Wang, H. M. Liu, T. D. Dao, M. Li, G. G. Liu, X. G. Meng, K. Chang, L. Shi, T. Nagao, J. H. Ye. *Adv. Mater.* 2016, **28** (19), 3703-3710.

6 Y. Qi, L. Song, S. Ouyang, X. Liang, S. Ning, Q. Zhang, J. Ye. *Adv. Mater*. 2019, **31** (25), 1903951 (8 pages).

7 Y. Qi, J. Jiang, X. Liang, S. Ouyang, W. Mi, S. Ning, L. Zhao, and J. Ye. *Adv. Funct. Mater*. 2021, **31** (22), 2100908 (8 pages).

8 M. Li, P. Li, K. Chang, T. Wang, L. Q. Liu, Q. Kang, S. X. Ouyang, J. H. Ye. *Chem. Commun*. 2015, **51**, 7645-7648.

9 Y. Li, M. Wen, Y. Wang, G. Tian, C. Wang, and J. Zhao. *Angew. Chem. Int. Ed.* 2020, **59**, 2-9.

10 H. Ge, Y. Kuwahara, K. Kusu, H. Yamshita. *J. Mater. Chem. A.* 2021, **9**, 13898-13907.